Bimetallic Au–Cu supported on ceria for PROX reaction: Effects of Cu/Au atomic ratios and thermal pretreatments

Xuemei Liao[a,b], Wei Chu[b], Xiaoyan Dai[b], Véronique Pitchon[a,*]

[a] ICPEES, Institut de Chimie et Procédés pour l'Energie, l'Environnement et la Santé, UMR 7515 du CNRS, Université de Strasbourg, ECPM, 25 rue Becquerel, 67087, Strasbourg, France
[b] Department of Chemical Engineering, Sichuan University, Chengdu, China

ARTICLE INFO

ABSTRACT

The influence of pretreatment (calcination or reduction), on bimetallic Au–Cu/CeO$_2$ catalysts with a fixed Au loading of 2 wt.% and an atomic Cu/Au ratio of 1/3, 1/1 or 3/1 was studied. The catalysts were prepared by direct anionic exchange of HAuCl$_4$ followed by a Cu(NO$_3$)$_2$ impregnation. Both pretreatment methods led to catalysts of significantly different structures and surface compositions. For the calcined samples, the presence of a copper oxide phase can be observed when the Cu/Au is 3/1, whereas, for the reduced catalysts, there is the formation of an Au–Cu alloy and of metallic copper due to the immediate decomposition of the copper precursor, which is able to be partially alloyed with gold. XPS reveals that the calcination led to the segregation of a CuO-rich phase on the surface, while in the case of reduction, the surface is not so Cu-enriched. All of the catalysts were evaluated by preferential oxidation of CO in the presence of hydrogen and compared with monometallic 2% Au/CeO$_2$ and 2% Cu/CeO$_2$. For all catalysts, it was found that irrespective of the atomic Cu/Au ratio, a reduction improves the CO conversion and CO$_2$ yield compared with monometallics while enhanced catalytic performances are only observed for the 1/3 Cu/Au atomic ratio of the calcined samples. The reduced Au–Cu bimetallics are stable with time on-stream contrary to the calcined one where the formation of carbonate-like species, responsible of a deactivation, is observed. Furthermore the reduced catalyst remained active even in the presence of CO$_2$ and H$_2$O in the gas stream

© 2013 Elsevier B.V. All rights reserved.

1. Introduction

For the future, hydrogen is being considered as a clean energy resource to replace polluting fossil fuels, notably for proton-exchange membrane fuel cells (PEMFC). However, for hydrogen to realize this potential a process leading to the efficient elimination of trace amounts of CO is required, an objective which can be achieved by the preferential oxidation reaction of CO (PROX). Current fundamental research for the removal of CO focuses on ceria-based catalysts such as monometallics (Au [1–8], Pt [9–14], Pd [15–17], and Ir [15,18]) and copper oxide [19–30], as well as a range of supported bimetallics (Au–Cu [31–34], Au–Ag [35], Au–Ni [36], Au–Pd [37], Au–Pt [38,39], Pt–Sn [40] and Pt–Fe [41]).

Due to the high activity of gold and the high selectivity of copper at low operation temperature, Au–Cu catalysts have been examined previously for the PROX reaction. Mozer et al. [31] used an Au-Cu/Al$_2$O$_3$ catalyst prepared by deposition–precipitation (DP) to load gold, subsequent addition of copper by impregnation

and finally calcination at 500 °C. The influence of the addition of copper was investigated and an optimal copper content for CO conversion was discovered. However, also suggested was that an excess of copper led to the blockage of the gold active sites. Liu et al. [34,42] studied an Au-Cu/SBA-15 catalyst prepared by direct reduction using NaBH$_4$ to reduce the solution precursor followed by calcination at 500 °C or reduction at 550 °C, which resulted in bimetallic nanoparticles displaying different structures. Exposure to air gave a copper-rich surface with a core–shell structure, whereas, exposure to hydrogen led to the formation of an alloy. The Au-Cu/SBA-15 catalyst with an alloy structure demonstrated a superior catalytic performance to that with the core–shell structure. The Au-Cu bimetallic catalysts above were supported on inert carriers such as alumina or silica and the enhancement observed in the reaction activity resulted from a synergetic effect occurring exclusively between gold and copper. Elsewhere, studies have focused on active supports such as ceria. For example, Fonseca et al. [33] found that the addition of CuO on Au/CeO$_2$ could not promote catalytic behavior at low temperature (below 100 °C).

The enhanced catalytic activity revealed for bimetallic catalysts, in comparative studies with monometallics, has been attributed to a variety of factors including the formation of nanostructures,

* Corresponding author. Tel.: +33 68852733; fax: +33 368852733.
E-mail address: pitchon@unistra.fr (V. Pitchon).

the atomic ratio, the particle size, the support and the nature of the catalyst surface. For example, a study of the effect of calcination temperature on bimetallic Au-Cu/TiO$_2$ catalysts found that by increasing the pretreatment temperature the resulting structural changes, from phase segregation to alloy formation, play a major role in enhancing the catalytic activity in propene epoxidation [43].

In the present work we have studied the effects of the Cu/Au atomic ratio as well as that of the nature of the pretreatment, using ceria as a support, on the catalytic performances in PROX reaction. Detailed analysis of the Au–Cu bimetallic structure as well as changes to the surface composition supplemented by XRD, HRTEM, HAADF-STEM, H$_2$-TPR and XPS data are proposed in order to establish the relationship between enhanced catalytic behavior and structure.

2. Experimental

2.1. Catalyst preparation

The bimetallic Au$_x$Cu$_y$/CeO$_2$ catalysts were prepared by a two-step method. The gold loading was fixed to 2% and the amount of copper was chosen in order to vary the atomic Au/Cu ratio (Cu/Au = 1:3, 1:1 and 3:1). In the first step, supported gold on ceria was prepared by Direct Anionic Exchange (DAE) as described in our previous studies [44–46]. A solution of HAuCl$_4$ (10^{-4} M) solution was heated to 70 °C and the exact amount of dried commercial ceria (Rhodia Actalys HSA 5, 95 m^2 g^{-1}) with a mesh size 125–250 μm was added under vigorous stirring for 1 h. Then 20 ml of a 4 M NH$_4$OH solution were introduced. The resulting slurry was filtered, washed several times with water and dried in an oven overnight at 110 °C. In a second step, the copper was loaded by impregnation. The Au–CeO$_2$ powder was introduced into an aqueous solution of Cu(NO$_3$)$_2$·3H$_2$O and stirred for 3 h. The solution was evaporated and the remaining solid dried in an oven at 110 °C for 3 h.

A fraction of the catalyst precursor was calcined under air by heating to 300 °C at 4 °C min^{-1}, holding at 300 °C for 4 h then cooling down to room temperature. The other fraction of the catalyst precursor was reduced in a furnace under a flowing 50% H$_2$/He gas mixture with a flow rate of 50 ml min^{-1}, heated to 300 °C at a rate of 10 °C min^{-1} where it was held for 2 h. The samples were named according to the nominal Cu/Au atomic ratios as Au$_3$Cu$_1$/CeO$_2$-C or R, Au$_3$Cu$_1$/CeO$_2$-C or R and Au$_3$Cu$_1$/CeO$_2$-C or R. The letters C or R stand for calcined or reduced catalysts, respectively.

For comparison, the monometallic Au/CeO$_2$ and CuO/CeO$_2$ catalysts were prepared by analogous DAE and IMP methods and finally calcined under air at 300 °C for 4 h. The targeted loading of gold and copper was 2%.

2.2. Characterisations

The gold and copper loadings of the calcined catalysts were determined by inductively coupled plasma emission spectroscopy (ICP-AES) at the CNRS center of chemical analysis.

The X-ray diffraction (XRD) patterns were recorded on a Bruker D8 advanced diffractom eter equipped with a Cu Kα radiation source (0.15418 nm) and Lynxieye detector, operating at 40 kV and 40 mA. A continuous mode was used to collect data in the 2θ range from 20° to 80° at a scanning speed of 0.02 or 0.008° min^{-1}.

High resolution transmission electron microscopy pictures (HRTEM) were obtained in Tecnai G2F20 S-Twin instrument; the samples were prepared by dispersing the solid in ethanol. One drop of the solution was placed onto a holey carbon film supported by a 300 mesh copper TEM grid and dried for 1 h. Analyses of the

core–shell structure were performed using a high-angle annular dark-field scanning TEM (HAADF-STEM) technique. Photographs and maps were taken on the same microscope at an accelerating voltage of 200 kV. In this case, few mg of catalyst were dispersed in ethanol and a drop was deposited on a holey Mo grid and dried 1 h under an infrared lamp.

The redox properties were evaluated by temperature programmed reduction under hydrogen (H$_2$-TPR) and carried out on a Micromeritics AutoChem II 2920 analyzer. Prior to the H$_2$-TPR test, each catalyst (50 mg) was loaded in a quartz U-tube and pretreated under argon with a flow rate of 50 ml min^{-1} at 150 °C for 30 min, then cooled under argon. H$_2$-TPR was performed by heating the catalysts at a rate of 10 °C min^{-1} up to 400 °C in a 10% H$_2$/Ar with a flow rate of 50 ml min^{-1}. A trap cooled with acetone/liquid-nitrogen slurry was placed before the TCD detector to retain the water produced.

The surface analysis was measured by X-ray photoelectron spectroscopy (XPS) on a Multilab 2000 spectrometer (Thermo VH Scientific) using Al Kα radiation (1486.6 eV). The aluminum anode was operated at an accelerating voltage of 15 kV, 15 mA, 20 V. The pressure in the analysis chamber was maintained in the range of 5 × 10^{-9} mbar. Spectra were obtained for the C 1s, O 1s, Au 4f, Ce 3d and Cu 2p regions. A peak area of each element was calculated using "Avantage" program from the company Thermoelectron. Shirley backgrounds were subtracted from the raw data to obtain the areas of each element.

Species formed on the surface of the catalysts under reacting mixture were analyzed by infrared spectroscopy on a Bruker Vertex 70 spectrometer, equipped with a DTGS detector, between 400 and 4000 cm^{-1}. Before testing the used catalysts, the background under air had been collected and the spectra of the fresh catalysts had been subtracted.

2.3. Catalytic test

The catalytic performances were evaluated at atmospheric pressure using a fixed bed quartz micro-reactor packed with 50 mg of catalyst diluted in 150 mg cordierite. The reaction mixture consisted of 1% CO, 1% O$_2$, 50% H$_2$ and He as a balance with a total flow rate of 200 ml min^{-1}. To investigate the effect of presence of carbon dioxide and water on catalytic performances in PROX, the reactant composition of 1% CO, 1% O$_2$, 35% H$_2$, 10% CO$_2$, 10% H$_2$O and He as a balance was studied. The flow rate was controlled using Tylan mass flow controllers. The temperature was monitored and controlled by a Eurotherm system. Analyses of CO, O$_2$ and CO$_2$ were performed using a Rosemount Infrared analyzer. The CO conversion and yield of CO$_2$ were calculated by the following equations:

- CO conversion (%)

$$X_{CO}(\%) = \frac{[CO_2]_{out}}{[CO]_{in}} \times 100$$

- Selectivity of oxygen to oxidize CO

$$S_{CO}(\%) = \frac{0.5 \times [CO_2]_{out}}{[O_2]_{in} - [O_2]_{out}} \times 100$$

- Yield of CO$_2$

$$Y(\%) = \frac{X_{CO} \times S_{CO}}{100}$$

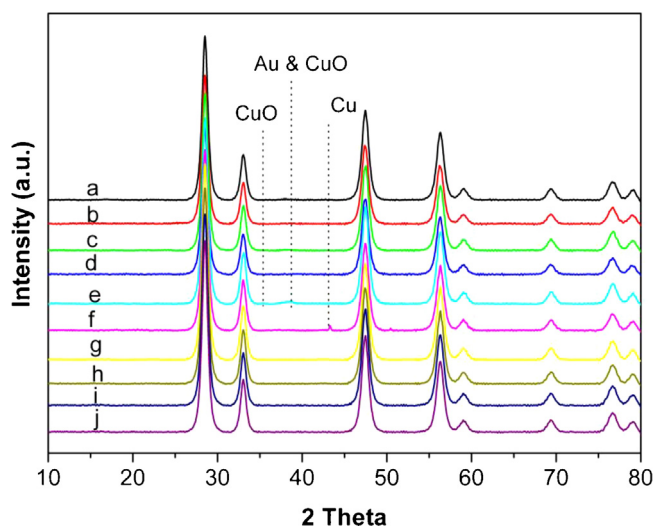where X_{CO}, S_{CO}, are the CO conversion, and selectivity of oxygen to oxidize CO, respectively.

Fig. 1. XRD patterns of supported monometallics and bimetallics. (a) Au_3Cu_1/CeO_2-C, (b) Au_3Cu_1/CeO_2-R, (c) Au_1Cu_1/CeO_2-C, (d) Au_1Cu_1/CeO_2-R, (e) Au_1Cu_3/CeO_2-C, (f) Au_1Cu_3/CeO_2-R, (g) Au/CeO_2-C, (h) Au/CeO_2-R, (i) CuO/CeO_2-C and (j) CuO/CeO_2-R.

Fig. 2. XRD patterns with a scanning speed of 0.008°/min for samples (a) Au_1Cu_3/CeO_2-C, (b) Au_1Cu_3/CeO_2-R, (c) Au/CeO_2-C, (d) Au/CeO_2-R, (e) CuO/CeO_2-C, (f) CuO/CeO_2-R.

3. Results

3.1. Catalysts compositions

The atomic ratios of bimetallic Au–Cu/CeO$_2$ calculated from the Au and Cu concentrations determined by ICP measurement are reported in Table 1. The theoretical gold loading was fixed to 2% and the atomic ratios of Cu/Au were varied from 0.33 to 3.00. The experimental gold loading for each sample is very close to the theoretical value, indicating that direct anionic exchange is a very effective and reproducible preparation method for depositing gold on ceria. The amount of copper deposited is slightly different from the nominal value but remains within the margin of experimental error.

3.2. Crystal phase of supported monometallics and bimetallics

The XRD patterns of Cu and Au monometallics and Au–Cu bimetallics are presented in Fig. 1. For all of the samples, the main diffraction peaks are present at 2θ = 28.59 (1 1 1), 33.13 (2 0 0), 47.56 (2 2 0), 56.43 (3 1 1), 59.18 (2 2 2), 69.53 (4 0 0), 76.83 (3 3 1) and 79.21 (4 2 0) and can be attributed to ceria with a face-centered cubic fluorite-type oxide structure [24,39]. In the monometallics there are no diffraction rays for gold or copper species phases due either to the high dispersion of the metal or to the fact that the gold and/or the copper concentrations are below the detection limits. On supported Au–Cu bimetallics, when the Cu/Au ratio increases from 1/3 to 3/1, the diffraction pattern of the CuO phase is observed only in the case of the calcined sample, i.e. Au_1Cu_3/CeO_2-C. While the copper loading of CuO/CeO_2-C is close to that of Au_1Cu_3/CeO_2-C, no diffraction ray of CuO is obtained in the case of monometallic sample CuO/CeO_2. A possible explanation for the detection of the CuO phase in Au_1Cu_3/CeO_2-C and not in CuO/CeO_2-C, although the amount of CuO is high enough to be detected, is the fact that the important parameter is the dispersion of CuO. This implies that the interaction between copper and ceria is weaker in Au_1Cu_3/CeO_2-C leading to a lower CuO dispersion than that of CuO/CeO_2. Another interesting point is the fact that for Au_1Cu_3/CeO_2-R reduced the characteristic diffraction rays of metallic copper are observed at 2θ = 43.4 and 50.5, suggesting the segregation of Cu clusters with a Cu bulk-like structure [47]. Bauer et al. [32] and Liu et al. [42] observed that 2θ of gold diffraction lines shift to a higher value under reduction pretreatment instead of simply implying the
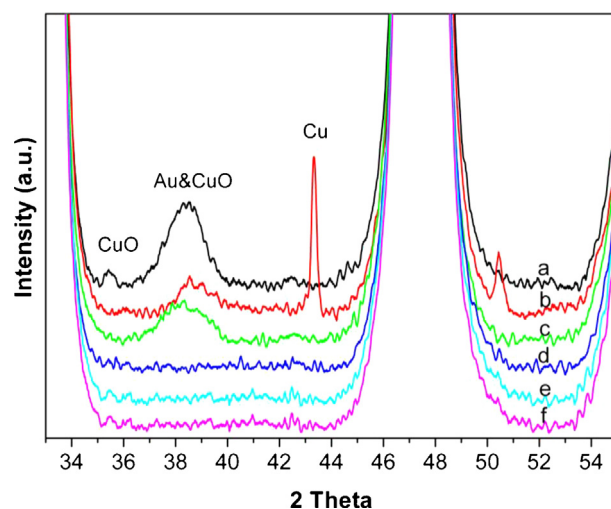
presence of metallic copper. To enhance this difference in the characteristic diffraction under reduction and to improve the resolution of the XRD pattern, the 6 samples (i.e. Au/CeO_2-C or R, CuO/CeO_2-C or R and Au_1Cu_3/CeO_2-C or R) were submitted to a longer scan time with a scanning speed of 0.008°/min as illustrated in Fig. 2. In this case, diffraction rays of gold at 2θ = 38.2° and copper oxide at 2θ = 35.6° and 38.8° appear clearly for samples Au/CeO_2-C and Au_1Cu_3/CeO_2-C. However, for the reduced sample Au/CeO_2-R, gold diffraction rays disappear totally suggesting a decrease of the gold particle size while in the case of Au_1Cu_3/CeO_2-R, Au and CuO phases are still displayed but with a weaker diffraction intensity and a shift in the diffraction angle to a higher value. This could result from the formation of a Au–Cu alloy [32]. To further address this point, high resolution transmission electron microscopy (HRTEM) was utilized to identify its formation.

3.3. High resolution transmission electron microscopy (HRTEM)

As inferred from XRD, the particle size of Au–Cu have is decreased for the reduced sample Au_1Cu_3/CeO_2-R. Average size of Au–Cu particle size of Au_1Cu_3/CeO_2-C and Au_1Cu_3/CeO_2-R calculated from the X-ray line (Fig. 2) are found to be equal to 4.9 nm and 3.5 nm. It is therefore important to confirm this fact by studying the particle by microscopy. However, due to the low contrast between gold/copper and ceria, it was not possible to count a large number of particles. The values were therefore deduced from particles where the lattice distance was clear on HRTEM images, as shown in Fig. 3a and b. Even in this case, it is important to point out that the values may not be representative of all the particles as this procedure was applied to c.a. 50 particles. From this sampling, the average particle sizes Au_1Cu_3/CeO_2-C and Au_1Cu_3/CeO_2-R are 3 ± 0.5 nm and 2 ± 0.5, respectively. These values are lower than those deduced from XRD but remain in the same range. Most important is the fact, that HRTEM confirmed that there is formation of an alloy Au_1Cu_3 for the reduced sample Au_1Cu_3/CeO_2-R.

3.4. HAADF-STEM

HAADF-STEM is a prevailing method for surface elementary composition and homogeneity of the composition of the particles in bimetallic samples. Image contrast in HAADF-STEM becomes brighter as the atomic mass of the element in the particle becomes heavier and hence it is possible to distinguish the presence of a

Table 1
Theoretical and experimental compositions of Au–Cu/CeO$_2$ bimetallics.

Sample	Au (%)^t	Cu (%)^t	Au (%)^a	Cu (%)^a	Cu/Au^t	Cu/Au^a
Au$_3$Cu$_1$/CeO$_2$-C	2.00	0.22	2.10	0.34	0.33	0.48
Au$_1$Cu$_1$/CeO$_2$-C	2.00	0.70	2.14	0.80	1.00	1.10
Au$_1$Cu$_3$/CeO$_2$-C	2.00	1.94	2.05	1.86	3.00	2.83
Au/CeO$_2$-C	2.00	–	2.10	–	–	–
Cu/CeO$_2$-C	–	2.00	–	1.94	–	–

Experimental error is ± 5%, –: not calculated.

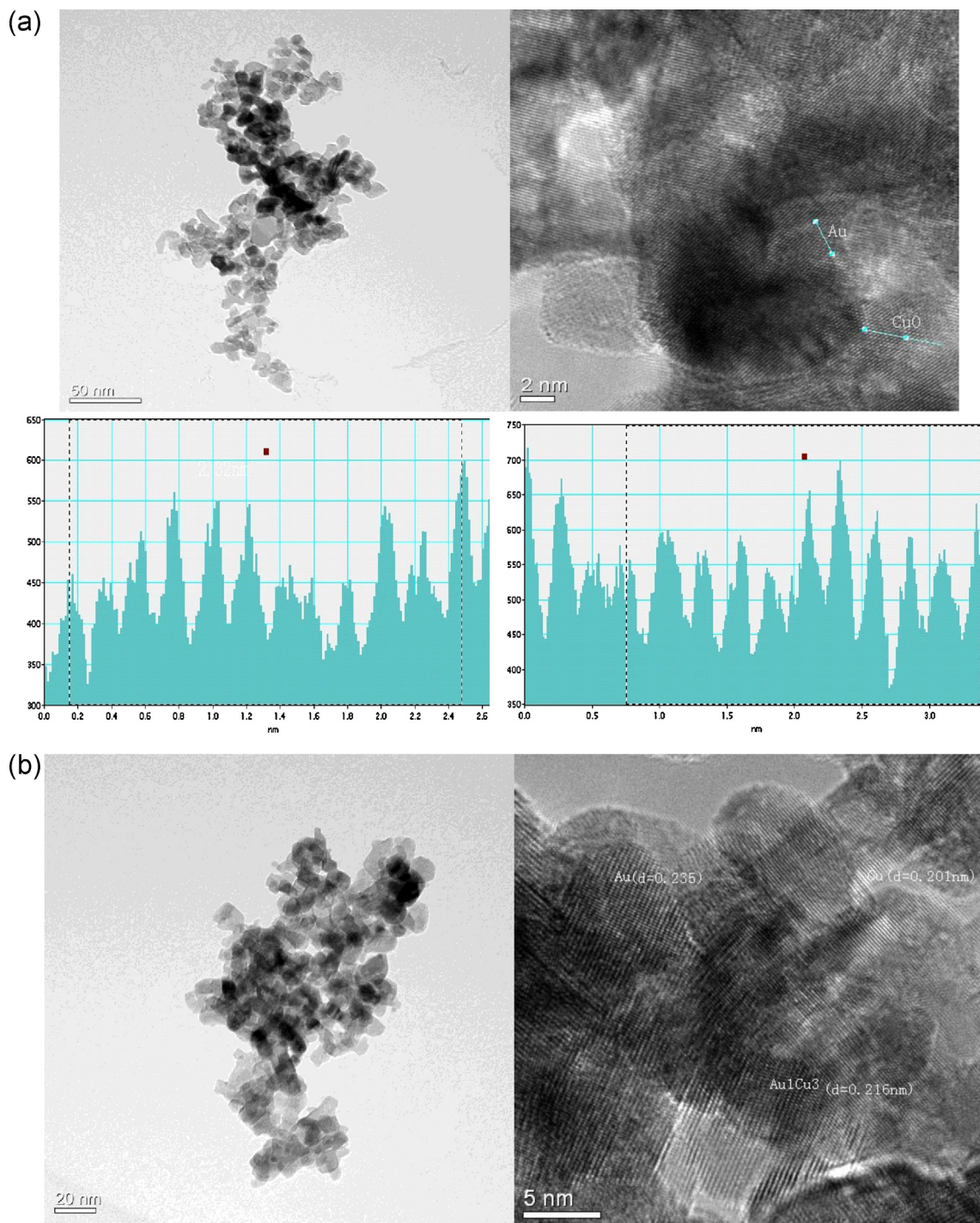^{t} Theoretical value.

^{a} From ICP.

Fig. 3. (a) HRTEM of Au$_1$Cu$_3$/CeO$_2$-C and the pixel intensity profiles for average lattice distance of CuO (left: 0.258) and gold (right: 0.232 nm). (b) HRTEM of Au$_1$Cu$_3$/CeO$_2$-R (lattice distance of each species are calculated as those shown in (a)).

core–shell structure. In order to study the elemental composition and distribution throughout the AuCu/CeO$_2$ samples, a detailed chemical analysis was carried out using EDS mapping. The images corresponding to the Au L-edge signal, Cu K-edge signal, O K-edge signals and Ce L-edge signal respectively were extracted for 2 zones of analysis for the Au$_1$Cu$_3$/CeO$_2$-C sample and Au$_1$Cu$_3$/CeO$_2$-R. These zones are represented within the red and yellow squares in Fig. 4a and c. For the sake of clarity, only the mapping corresponding to the red square zones are presented in Fig. 4b and d respectively.

According to the EDS spectrum, sample: Au$_1$Cu$_3$/CeO$_2$-C (Fig. 4a and b) contain about 0.10 of Au/Cu atomic ratio, which is rather lower than the theoretical ratio–i.e. 0.32. It can also be seen that Au signal is smaller than that of Cu in the confined maps (red square), possibly due to the fact that Au is covered by CuO or to the presence the large segregated CuO islands resulting from the weak interaction between copper and ceria as shown inferred by XRD. Comparing Cu signal to Ce signal, the O signal is mainly originated

from copper oxide. In the Au$_1$Cu$_3$/CeO$_2$-R (Fig. 4c and d), two maps are investigated and each Au L-edge, Cu K-edge, Ce L-edge and O K-edge in the both maps are displayed. It can be seen from the EDS spectrum, each map contains both gold and copper and also have an atomic ratio of Au/Cu of 0.38 very close to the theoretical one of 0.33. In the confined maps, the Au L-edge and Cu K-edge signals are homogenous. From Ce L-edge signal, it can be deduced that Au and Cu are located homogenously on the ceria support. The interactions between gold and ceria as well as those between copper and ceria are stronger than that of the calcined sample. The small O signal as compared with that of Au$_1$Cu$_3$/CeO$_2$-C is mainly originated from ceria, which directly support the presence of metallic copper as observed by XRD.

3.5. Temperature-programmed reduction

H$_2$-TPR profiles of 2% Au/CeO$_2$, 2% CuO/CeO$_2$ and of the bimetallic Au-Cu catalysts with various compositions are displayed in Fig. 5.
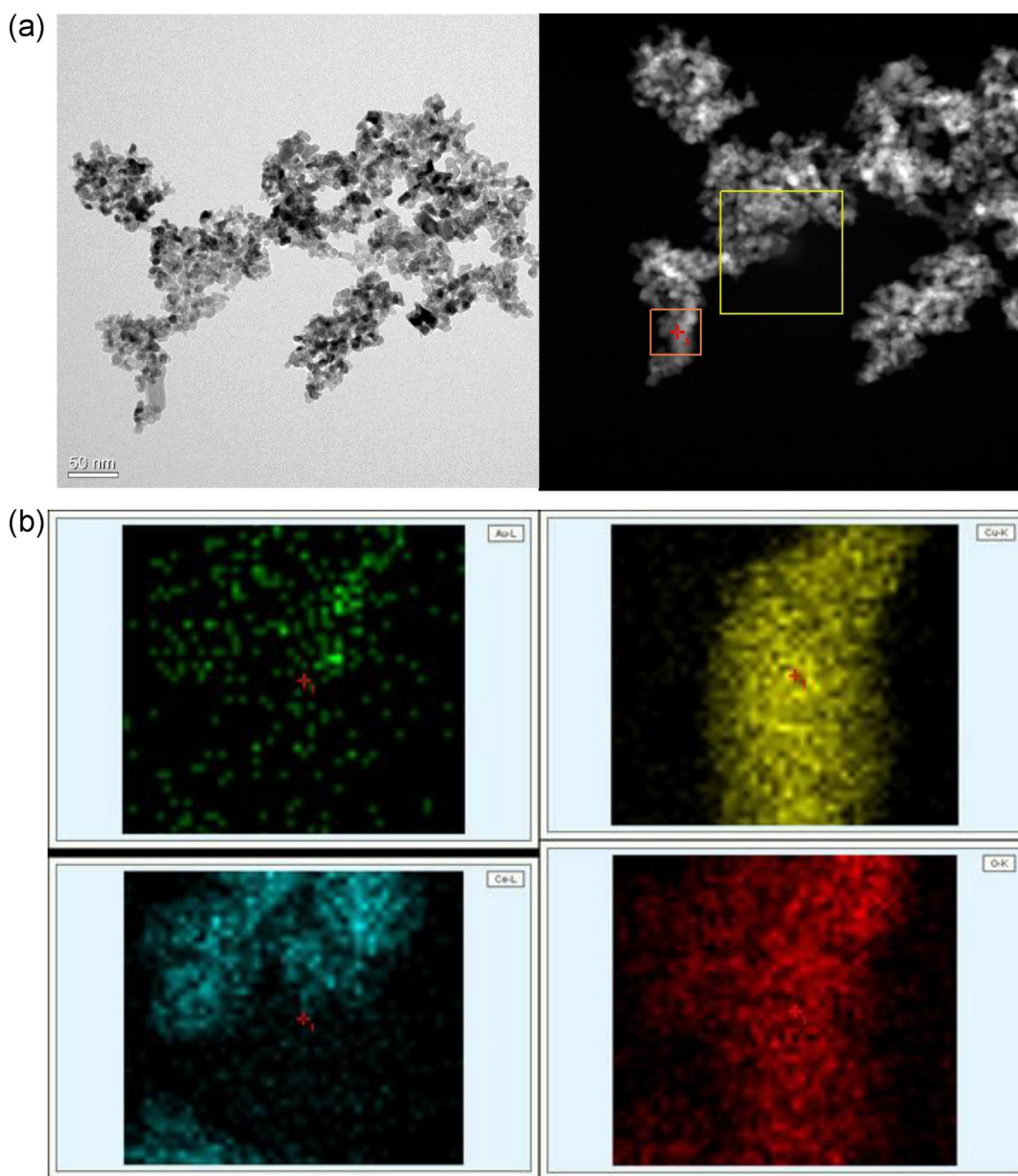

Fig. 4. (a) and (b) Zones of analysis by HRAAF of Au$_1$Cu$_3$/CeO$_2$-C and corresponding mapping image or red zone. (c) and (d) Zones of analysis by HRAAF of Au$_1$Cu$_3$/CeO$_2$-R and corresponding mapping image or red zone. (For interpretation of the references to color in this figure legend, the reader is referred to the web version of the article.)
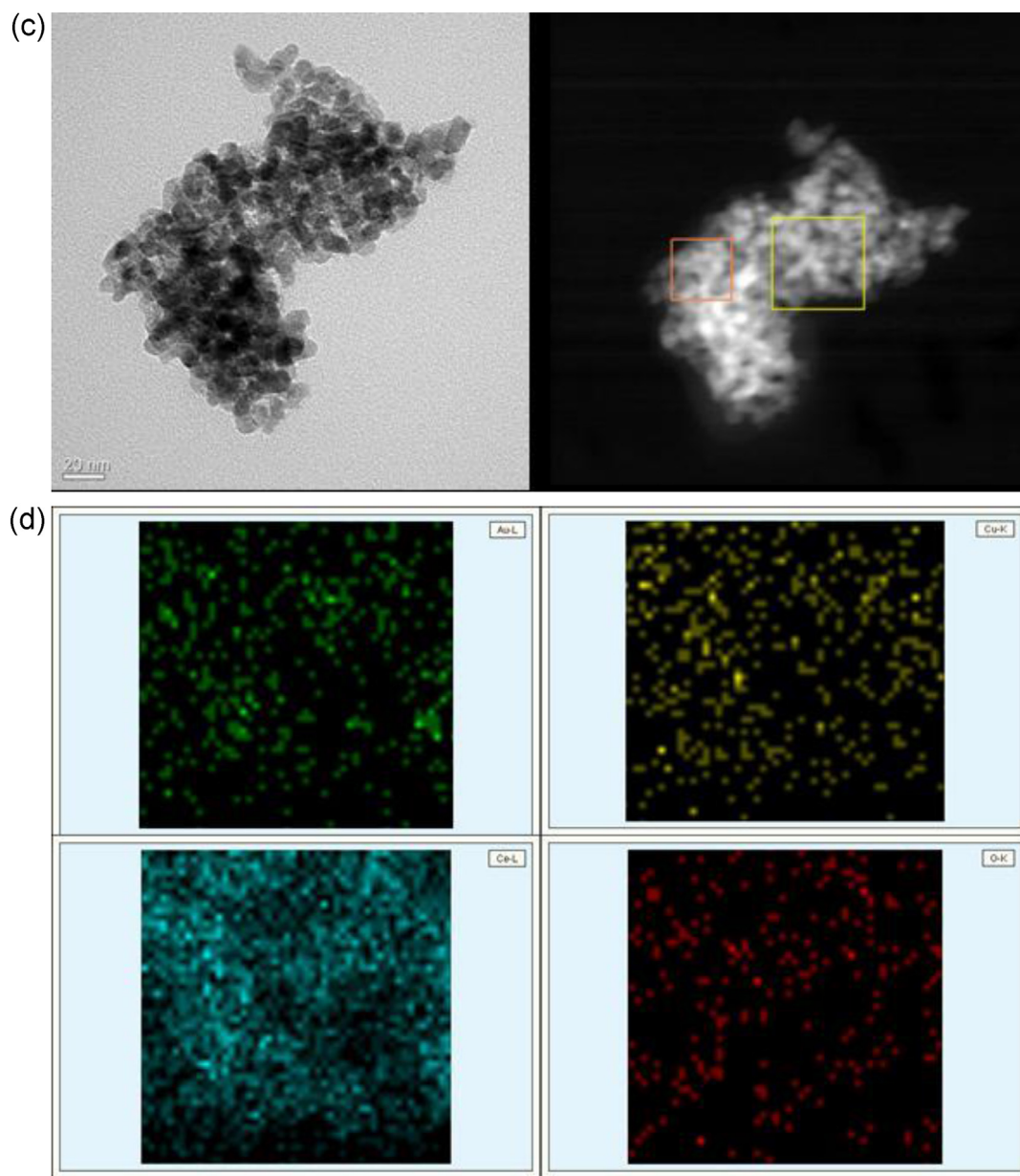
(c)

(d)

Fig. 4. (Continued)

The TPR profile of Cu/CeO_2 presents two reduction peaks centered at about $140\,^{\circ}C$ and $162\,^{\circ}C$, indicating the existence of two CuO species; highly dispersed CuO on the ceria surface and isolated Cu ions, respectively [24,48]. For the Au/CeO_2 catalyst, the TPR profile reveals a large reduction zone over a wide temperature range, starting from $50\,^{\circ}C$ and ending at $180\,^{\circ}C$. This reduction phenomenon has been reported previously and explained as the reduction of adsorbed oxygen on both gold and surface ceria [49,50]. The reduction profiles of bimetallic $Au-Cu/CeO_2$ catalysts present in all cases two peaks of reduction as shown in Fig. 5c–e, but the reduction temperature and the amount of H_2 consumed depend upon the Cu/Au atomic ratio. When the Cu/Au ratio increases, the reduction peaks at both high and low temperature shift to higher temperatures. In most cases, gold undergoes auto-reduction which explains why no corresponding reduction pattern is observed under H_2 [44]. Therefore, we postulate that the reduction profile results only from the reduction of CuO and CeO_2. The relatively low reduction temperature indicates that the reduction is assisted by reduced

Table 2
Results of H_2-TPR analysis of monometallic and bimetallic catalysts.

Sample	T_{max} $(^{\circ}C)$	Total H_2 uptake $(\mu mol\,g^{-1})$	Theoretical H_2 uptake $(\mu mol\,g^{-1})$ Cu^{2+} to Cu°	H_2 uptake of CeO_2 $(\mu mol\,g^{-1})$ Ce^{4+} to Ce^{3+}
CuO/CeO_2-C	163	44.6	16.0	28.6
Au/CeO_2-C	101	14.3	–	–
Au_3Cu_1/CeO_2-C	153	15.2	2.6	12.6
Au_1Cu_1/CeO_2-C	132	23.6	6.2	17.4
Au_1Cu_3/CeO_2-C	159	25.5	14.7	10.8
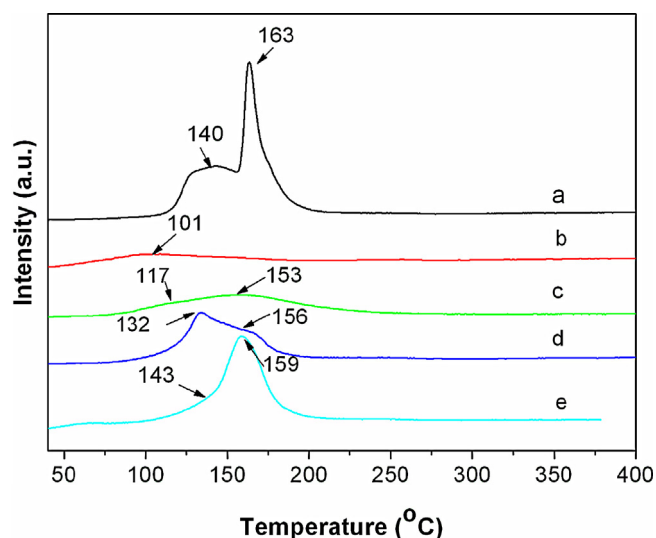
Fig. 5. TPR profiles of supported monometallic and bimetallic catalysts; (a) CuO/CeO_2-C, (b) Au/CeO_2-C, (c) Au_3Cu_1/CeO_2-C, (d) Au_1Cu_1/CeO_2-C, (e) Au_1Cu_3/CeO_2-C.

Fig. 6. Comparison of bulk and XPS atomic Cu/Au ratios on bimetallic catalysts calcined (■) or reduced (●).

gold which favors the adsorption of molecular hydrogen which subsequently becomes involved in the reduction of both CuO and CeO_2 at those temperatures. For example, the low reduction temperature peak for Au_3Cu_1/CeO_2 is centered at c.a. 117 °C, whereas, for samples of Au_1Cu_1/CeO_2 and Au_1Cu_3/CeO_2 those values are c.a. 133 °C and c.a. 144 °C, respectively, while the high temperature peak for Au_3Cu_1/CeO_2 shifts to 153 °C and that for Au_1Cu_3/CeO_2 to 160 °C. These results are different from those reported by Chimentao et al. [47] who observed that the increase of copper in Au–Cu bimetallics supported on TiO_2 led to the decrease of the reduction temperature. This disagreement may result from the different preparation methods employed. In our preparation process, conversely to the work cited above for which Au and Cu were co-impregnated in order to favor an alloy formation, Au was loaded first on CeO_2 and Cu was then impregnated on CeO_2 modified by Au. Theoretically, it can be speculated that when Cu is added in a second step, it can cover either partially or completely the gold cluster, the low reduction temperature could then be attributed to the highly dispersed CuO interacting with CeO_2, while the higher reduction temperature could be related to an interaction with larger CuO particles. More interesting is the case of the Au_1Cu_3/CeO_2-C sample for which the area at high reduction temperature centered at 159 °C is much larger than that of the low reduction temperature, i.e. at 143 °C, indicating the presence of larger CuO particles in Au_1Cu_3/CeO_2-C, as implied by the XRD pattern.

The H_2 uptake evaluated from an integration of the TPR curves is reported in Table 2. The amount of H_2 globally consumed for each Au-Cu bimetallic catalyst increases as the copper loading increases. Moreover, for all the bimetallics this amount exceeds largely the one required for the complete reduction of Cu^{2+} ion
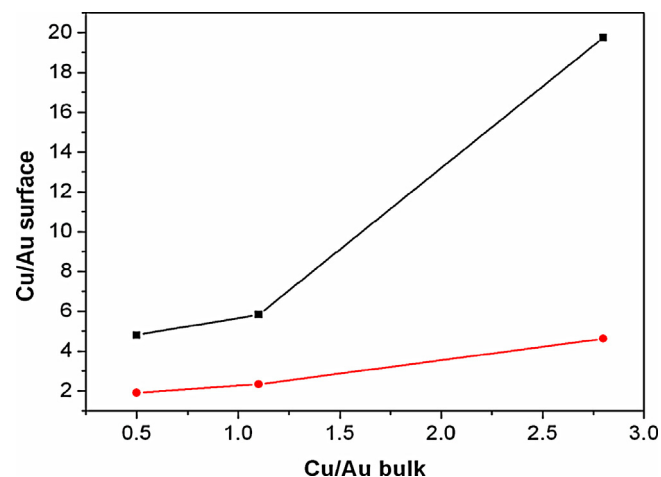
to Cu^0, suggesting that some reduction of CeO_2 occurs at low temperature. A similar phenomenon has also been observed for copper-ceria catalysts [24]. The discrepancy between theoretical and experimental values for H_2 uptake can be explained by the reduction of support surface by hydrogen spillover. In the present case, the amount of H_2 consumed by ceria increases with the increasing of copper loading in bimetallics, i.e. for Au_3Cu_1/CeO_2 and Au_1Cu_1/CeO_2 with 12.6 μmol and 17.4 μmol, respectively. However, for the Au_1Cu_3/CeO_2 sample, due to presence of larger copper oxide particles as revealed by XRD, the hydrogen spillover weakens and the amount of H_2 consumed by ceria decreases to 10.8 μmol, which may strongly influence catalytic performance.

3.6. XPS analysis

3.6.1. Surface compositions of bimetallics

X-ray photoelectron spectroscopy is a technique well-known for characterizing the surface compositions of multi-component materials [51–56]. In the present study, it is very convenient to express the surface compositions of the Cu–Au bimetallics; these XPS data are summarized in Table 3 for all of the bimetallic Cu-Au catalysts whether calcined or reduced. Clearly, for all catalysts the gold surface amount is much lower than the bulk value of 2% whatever the thermal treatment. For the calcined samples, the gold percentages decrease with increasing Cu/Au ratios. When the atomic ratio of Cu/Au is to 3/1, the gold surface percentage is the smallest, with a value 0.29%. In contrast, the copper surface percentages increase with an increase in Cu/Au ratio for all of the calcined catalysts and it is worth noting that the surface of the calcined catalysts is enriched in copper. The degree of this surface copper enrichment is governed by the ratio Cu/Au and this value increases with increasing the nominal Cu/Au ratio. Surprisingly, when the nominal ratio of Cu/Au reaches 3/1, the surface composition of Cu/Au is 19.76,

Table 3
Summary of surface and bulk composition of Au–Cu bimetallics on ceria.

Sample	Cu/Au[a] (ratio)	Au[b] (%)	Cu[b] (%)	Ce[b] (%)	O[b] (%)	Cu/Au[b] (ratio)
Au_3Cu_1/CeO_2-C	0.48	0.62	2.98	20.55	75.85	4.81
Au_3Cu_1/CeO_2-R	0.48	0.77	1.47	23.08	74.68	1.91
Au_1Cu_1/CeO_2-C	1.10	0.53	3.09	23.91	72.47	5.83
Au_1Cu_1/CeO_2-R	1.10	0.86	2.00	25.35	71.79	2.33
Au_1Cu_3/CeO_2-C	2.83	0.29	5.73	20.68	73.30	19.76
Au_1Cu_3/CeO_2-R	2.83	0.67	3.10	22.63	73.60	4.63

[a] Actual value determined by ICP.
[b] Surface value determined by XPS.

which is much higher than that of the other two calcined catalysts. For the case of the Au_1Cu_3/CeO_2-C sample, the suggestion can be made that most of the Au phase is covered by a Cu phase. There is a substantial enrichment of copper on the surface with respect to the bulk values. Similar results were observed for the case of bimetallic particles possessing a core–shell structure [57,58].

In comparison with the calcined bimetallic catalysts, the surface copper percentages and Cu/Au ratios decrease dramatically in all of the reduced samples. Fig. 6 displays a comparison of surface and bulk atomic Cu/Au ratio following calcination or reduction of the catalysts. When the bimetallic precursors are reduced rather than being calcined, the surface atomic Cu/Au ratios are closer to that of the bulk, with the exception of the sample of higher Cu content (i.e. Cu/Au = 3/1). This approximation of Cu/Au XPS ratios to bulk ratios depends on nominal ratios. Smaller nominal Cu/Au ratios can result in Cu/Au XPS ratios close to that of the bulk

values. Generally, the reduction pretreatment leads to a high mobility of a metal in a bimetallic and a fraction of this metal can easily be alloyed, while the other fraction remains as an oxide [59–61]. For the Au_1Cu_3/CeO_2 sample, the situation appears to be similar: following reduction, a part of the copper is metallic and dissolved in the AuCu alloy particles, another part may be still in an oxidic state (see XRD results). Due to the presence of highly mobile metallic Cu and the diffusion of Cu during the reduction pretreatment, there is an AuCu alloy formation, which leads to Cu/Au XPS ratios close to the bulk values. Changes of surface Cu/Au ratios can lead to different catalytic behavior, as discussed in the following section.
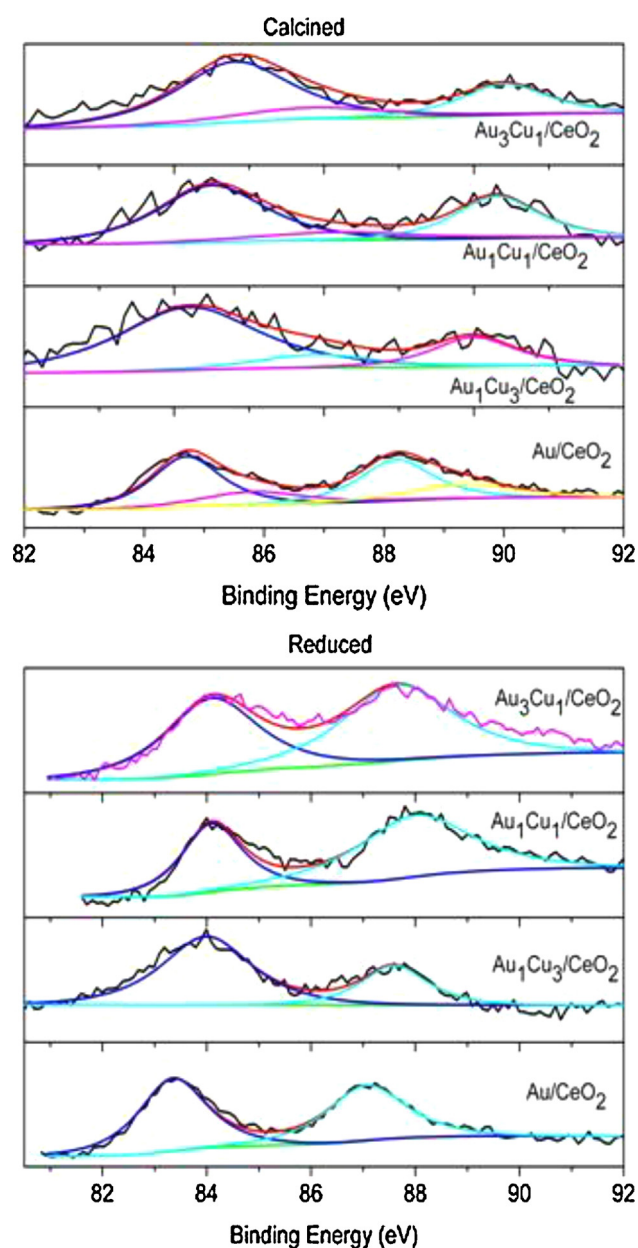

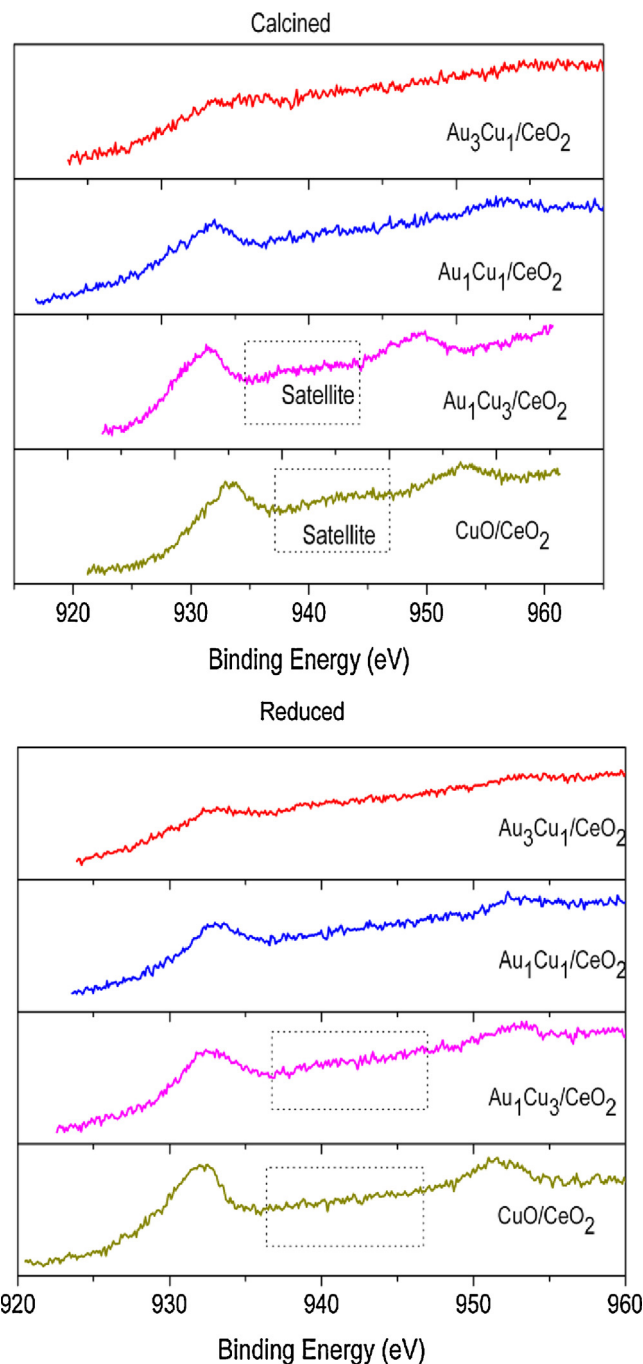**Fig. 7.** Au 4f XP spectra of CeO_2 supported monometallic and Au–Cu bimetallic catalysts, calcined or reduced.

Fig. 8. Cu 2p XP spectra of CeO_2 supported monometallic and Au–Cu bimetallic catalysts.

3.6.2. Surface chemical states of gold, copper and cerium

Fig. 7 represents the experimentally measured and fitted Au 4f spectra of the calcined or reduced monometallic Au/CeO_2 and bimetallic $Au-Cu/CeO_2$ catalysts. For the calcined samples, the two Au 4f7/2 values of BE 84.5 ± 0.3 eV and 85.8 ± 0.2 eV components can be assigned to Au^0 and Au^{1+} species. A small fraction of oxidized Au^{1+} species is found in the calcined samples as displayed by the relative distribution of Au species in Table 4. When the amount of copper is increased, the peak positions of metallic gold are shifted towards lower BE at 84.5 eV for Au_1Cu_1/CeO_2-C and 84.2 eV for Au_1Cu_3/CeO_2-C respectively. A shift to lower BE in XPS is usually associated with an increased electron density or a reduction to a lower valence state. These results indicate that there is an electron transfer leading to an increased electron density around the gold. In the case of reduced samples, only one type of gold species in the form of Au^0 is observed with BE at c.a. 84.0 ± 0.3 eV, (Table 4).

In Fig. 8, the X-ray photoelectron spectra in the Cu 2p region for calcined or reduced monometallic copper and bimetallic gold and copper on ceria are presented, their BE being summarized in Table 4. The calcined samples exhibit typical values for Cu^{2+} with main peaks of Cu 2p$_{3/2}$ appearing c.a. 933 eV, together with weak satellites at higher BE. However, upon reduction, the satellites in the Cu 2p core level disappear and all of the Cu 2p$_{3/2}$ peaks are shifted towards lower BE. The reduced monometallic CuO/CeO_2 catalyst reveals a peak at 932.2 eV value which is lower by 1.2 eV when compared with the calcined monometallic CuO/CeO_2. The reduced bimetallics Au_3Cu_1/CeO_2-R, Au_1Cu_1/CeO_2-R and Au_1Cu_1/CeO_2-R display BE typical of Cu 2p3/2 at 932.9, 933.0 and 932.6 eV, respectively, values which decrease by 0.5–0.7 eV when compared with the calcined bimetallic Au–Cu. This loss of satellites and shift towards lower BE with respect to the reduced samples clearly indicates a reduction of Cu^{2+} to a lower oxidation or metallic state as confirmed by XRD and by HRTEM. An attempt to distinguish deeply the Cu^0 and Cu^+ could be addressed further by Auger or CO-FTIR characterization.

The Ce 3d region XP spectra of calcined and reduced samples are shown in Fig. 9a, an example of the deconvolution being given Fig. 9b. At least six peaks at c.a. 883, 889, 898, 901, 908 and 917 eV are observed for both calcined and reduced samples and they are assigned to Ce 3d$_{5/2}$ 4f^2, Ce 3d$_{5/2}$ 4f^1, Ce 3d$_{5/2}$ 4f^0, Ce 3d$_{3/2}$ 4f^2, Ce 3d$_{3/2}$ 4f^1 and Ce 3d$_{3/2}$ 4f^0, respectively for Ce^{4+} species in CeO_2. In addition to these six peaks, the reduced bimetallic $Au-Cu/CeO_2$ samples exhibit an obvious shoulder at c.a. 885 eV due to the formation of Ce^{3+} species. As displayed in Table 4, all samples display the presence of Ce^{3+} which might be due either to the thermal treatment during the preparation, or the radiation in the analysis chamber. The concentration of Ce^{3+} in the reduced bimetallic samples is significantly enhanced.

3.7. Catalytic performances in PROX

Catalytic performances were evaluated in PROX under a rich hydrogen concentration in the temperature range of 40–300 °C for
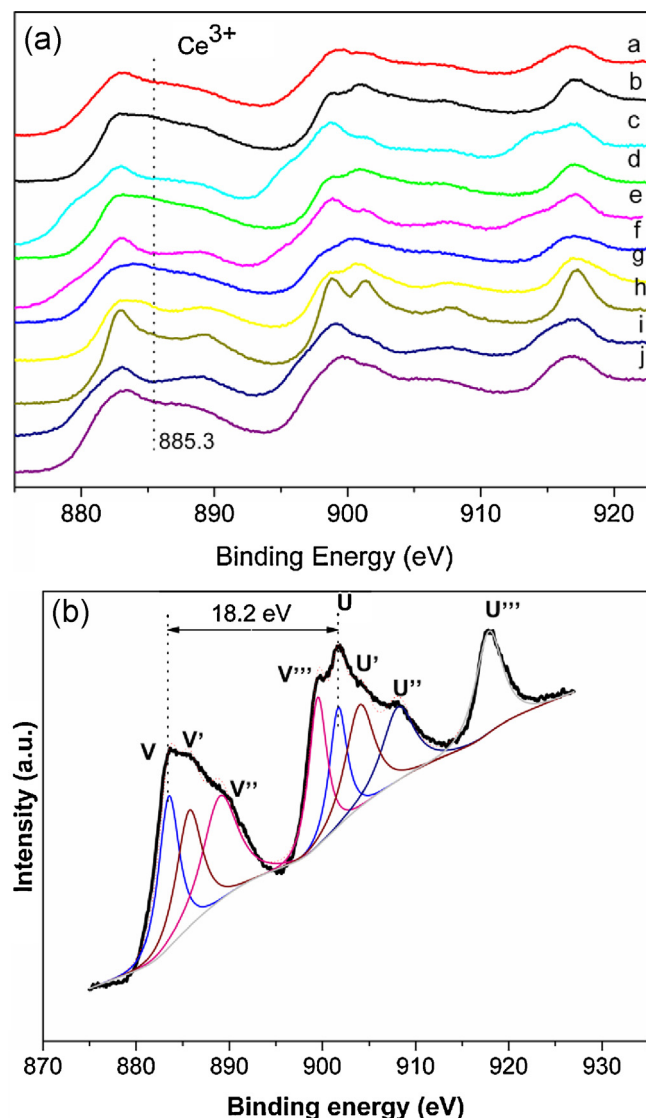

Fig. 9. Ce 3d spectra of CeO_2 supported monometallic and Au–Cu bimetallic cataysts. (a) Au_3Cu_1/CeO_2-C, (b) Au_3Cu_1/CeO_2-R, (c) Au_1Cu_1/CeO_2-C, (d) Au_1Cu_1/CeO_2-R, (e) Au_1Cu_3/CeO_2-C, (f) Au_1Cu_3/CeO_2-R, (g) Au/CeO_2-C, (h) Au/CeO_2-R, (i) CuO/CeO_2-C, (j) CuO/CeO_2-R. (b) Example of the deconvolution of Ce 3d of Au_1Cu_1/CeO_2-R.

monometallic Au/CeO_2-C and CuO/CeO_2-C and for the bimetallic $Au-Cu/CeO_2$ (C or R) catalysts. As reported in the literature [12], the monometallic nano-gold is more active at low temperature but less selective in comparison with nano-copper oxide, which exhibits a lower activity at low temperature but which is more selective at high temperature. The different catalytic activities of monometallic Au/CeO_2-C and CuO/CeO_2-C catalysts are presented in Fig. 10a.

Table 4
Summary of binding energies of Au 4f$_{7/2}$, Cu 2p$_{3/2}$ and concentrations of Ce^{3+}.

Sample	Au^0 4f$_{7/2}$ (eV)	Au^+ 4f$_{7/2}$ (eV)	Cu 2p$_{3/2}$ (eV)	Ce^{3+} 3d$_{5/2}$ (%)
Au_3Cu_1/CeO_2-C	84.8	86.0 (17.4%)	933.6	18.5
Au_1Cu_1/CeO_2-C	84.5	86.1 (17.3%)	933.5	14.6
Au_1Cu_3/CeO_2-C	84.2	85.9 (14.7%)	933.2	14.3
Au/CeO_2-C	84.7	86.1 (27.1%)	–	16.8
CuO/CeO_2-C	–	–	933.4	14.0
Au_3Cu_1/CeO_2-R	84.2	–	932.9	20.4
Au_1Cu_1/CeO_2-R	84.0	–	933.0	25.7
Au_1Cu_3/CeO_2-R	84.1	–	932.6	24.5
Au/CeO_2-R	83.7	–	–	17.7
CuO/CeO_2-R	–	–	932.2	17.5
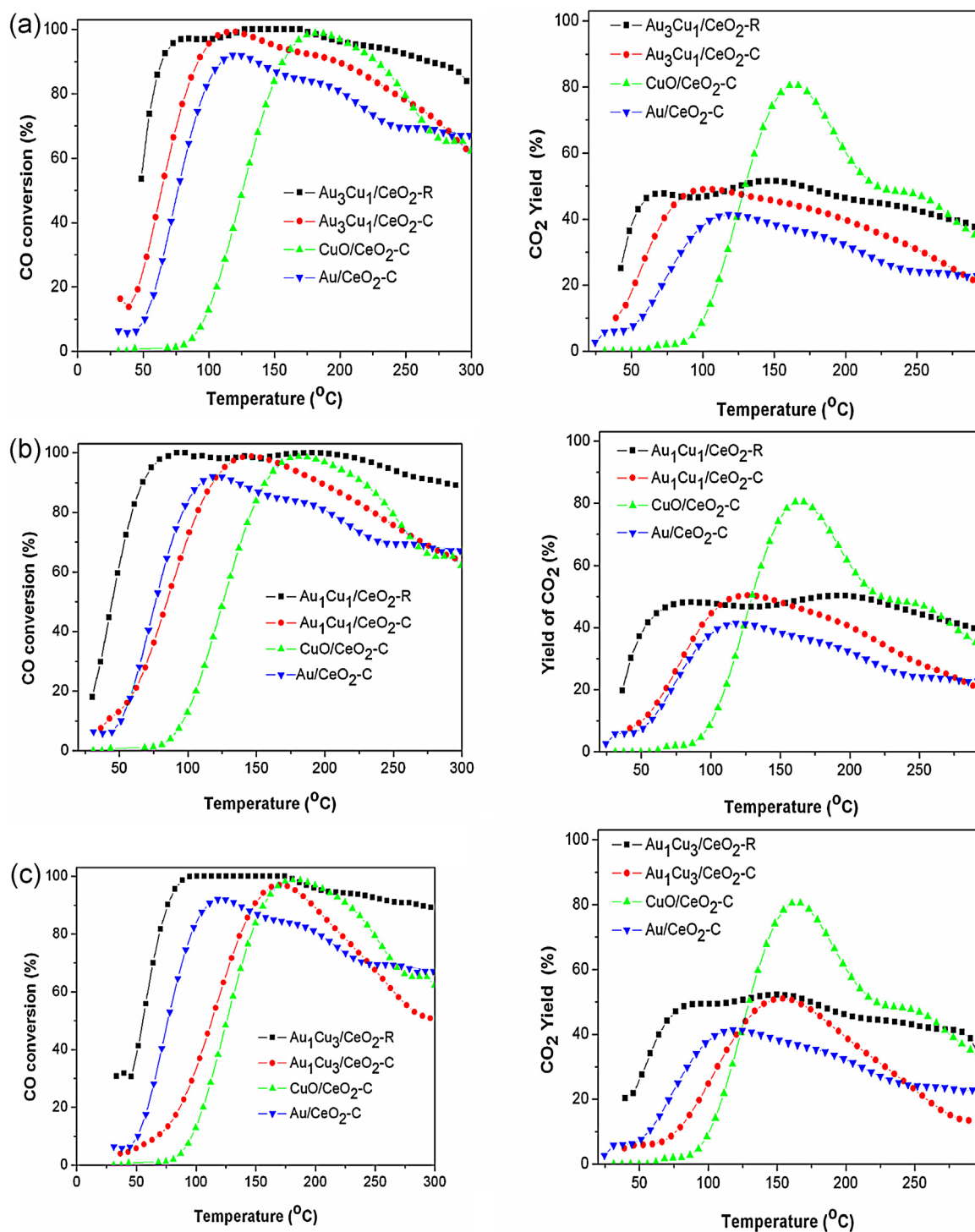
Fig. 10. (a) CO conversion and CO_2 yield on Au_3Cu_1/CeO_2 (R or C) compared with Au/CeO_2 and CuO/CeO_2. (b) CO conversion and CO_2 yield on Au_1Cu_1/CeO_2 (R or C) compared with Au/CeO_2 and CuO/CeO_2. (c) CO conversion and CO_2 yield on Au_1Cu_3/CeO_2 (R or C) compared with Au/CeO_2 and CuO/CeO_2.

As expected, the Au/CeO_2-C catalyst displays a much higher activity than that of CuO/CeO_2-C. At 110 °C, the conversion of CO is 88% on Au/CeO_2-C and 18% for CuO/CeO_2-C. However, at higher temperature (110–180 °C) the CO conversion on Au/CeO_2-C decreases to c.a. 80%, while CO conversion on CuO/CeO_2 exhibits an increase to a maximum value of 99%. Meanwhile, for this temperature range, the CO_2 yield for CuO/CeO_2-C can achieve a maximum value of 95%, which by far exceeds that of Au/CeO_2-C for which a maximum of

c.a. 40% is obtained at 110 °C. It is worth noting that the CO conversion on reduced monometallic Au or Cu is not enhanced comparing with the calcined monometallics.

3.7.1. Effect of Cu/Au atomic ratios in calcined bimetallics

The performances of the calcined catalysts containing different Cu/Au ratios are presented in Fig. 10a–c. Among these samples, differences appear both in terms of CO conversion and CO_2 yield.

Regarding CO conversion below 100 °C, catalysts can be ranked as:

$$Au_3Cu_1/CeO_2\text{-}C > Au/CeO_2\text{-}C > Au_1Cu_1/CeO_2\text{-}C$$

$$> Au_1Cu_3/CeO_2\text{-}C > CuO/CeO_2\text{-}C.$$
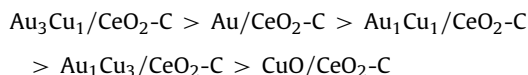
These catalysts, it should be recalled, contained virtually the same gold loading (see Table 1). At 75 °C, the Au_3Cu_1/CeO_2-C catalyst exhibits 68% CO conversion, which is the highest of all the catalysts, whereas on Au/CeO_2-C CO a conversion of only c.a. 48% is reached. At the same temperature, these values are of 38% for Au_1Cu_1/CeO_2-C and of 13% for Au_1Cu_3/CeO_2-C. The reason for the different catalytic activities at low temperature can be associated with both structure and surface composition of these Au–Cu bimetallics. When the temperature increases from 100 to 250 °C, the conversion of CO on bimetallic Au–Cu catalysts increases and exceeds CO conversion of Au/CeO_2. Each of the bimetallic catalysts reaches a maximum CO conversion at a different temperature. In the temperature range of 100–250 °C, the catalytic performances can be ordered:

$$Au_3Cu_1/CeO_2\text{-}C > Au_1Cu_1/CeO_2\text{-}C > Au_1Cu_3/CeO_2\text{-}C$$
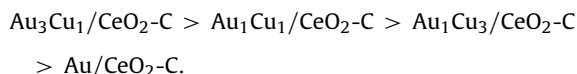
$$> Au/CeO_2\text{-}C.$$

Regarding the catalyst selectivity, it is interesting to note that the Au–Cu ratios have a strong influence on the CO_2 yield. At a reaction temperature of 100 °C, the Au_3Cu_1/CeO_2-C catalyst exhibits 50% of CO_2 yield, while the Au_1Cu_1/CeO_2-C, Au/CeO_2-C, Au_1Cu_3/CeO_2-C and CuO/CeO_2-C exhibit 42, 38, 28 and 8% of CO_2 yield respectively.

3.7.2. Effect of atomic Cu/Au ratios in reduced bimetallics

The effect of modifying the Cu/Au atomic ratio in reduced bimetallics on CO conversion and CO_2 yield are compared in Fig. 10a–c. In general, these reduced bimetallic catalysts, irrespective of their Cu/Au atomic ratio, perform better in the operation temperature range of the fuel cell when compared with the calcined monometallic and bimetallic catalysts. The effect of the Cu/Au atomic ratio of the reduced catalysts on CO conversion and CO_2 yield within the temperature range 50–90 °C follows the order:

$$Au_1Cu_1/CeO_2\text{-}R > Au_3Cu_1/CeO_2\text{-}R > Au_1Cu_3/CeO_2\text{-}R.$$
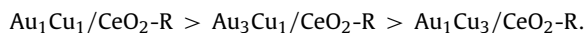
When the temperature increases a maximum for CO conversion is achieved and maintained across a wide range of temperatures. Continuing to increase temperature provokes a small decrease in CO conversion due to the oxidation of hydrogen. The Au_1Cu_1/CeO_2-R catalyst, it is worth noting, exhibits the best catalytic performance of all the reduced bimetallics over the temperature range 100–250 °C. The maximum value of CO conversion can reach 100% for all of the reduced catalysts while Au_3Cu_1/CeO_2-C is the only calcined catalyst to obtain this value.

When the effect of calcination and reduction pretreatments are compared by light-off curves, the CO conversion and CO_2 yield plots are seen to shift to lower temperature and that for the reduced catalysts the operation window becomes wider. This present work has found that among the monometallic and bimetallic catalysts, the Au_1Cu_1/CeO_2-R catalyst demonstrates the best performance over the temperature range of 50–100 °C and presents the widest operation window, making the Au_1Cu_1/CeO_2-R catalyst the most suitable for the CO-PROX application at similar temperatures to that of fuel cell operation.

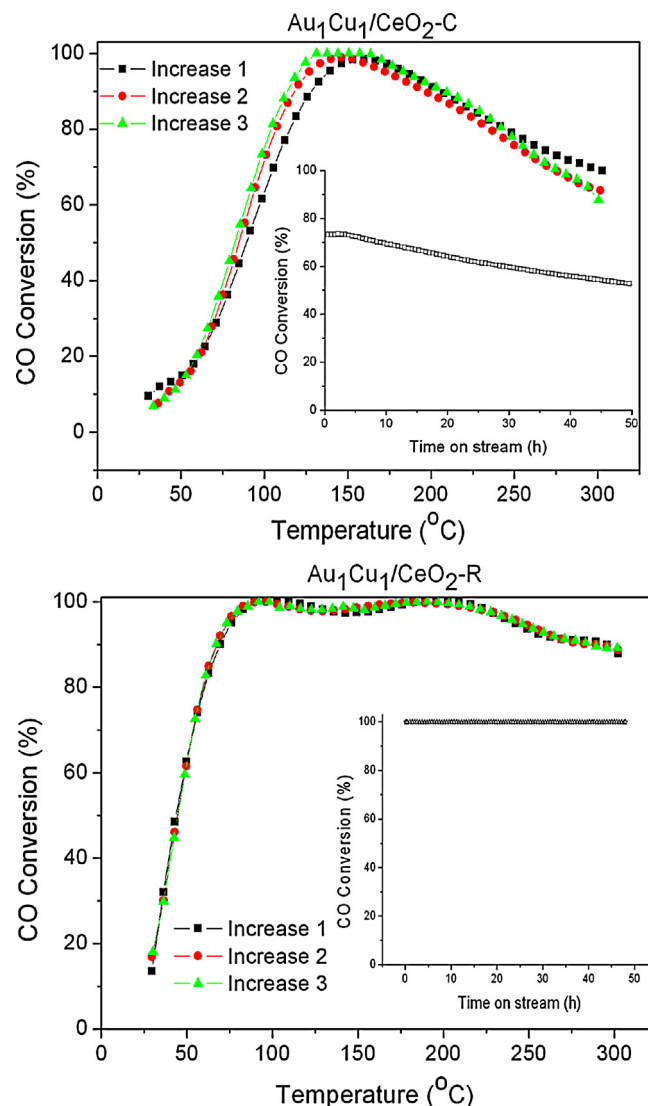Fig. 11. Effect of calcination or reduction on the stability of Au_1Cu_1/CeO_2 catalyst under PROX reaction atmosphere. Inserts: Time on stream over 48 h.

3.7.3. Stabilities of the bimetallic Au_1Cu_1/CeO_2-C and Au_1Cu_1/CeO_2-R catalysts

Fig. 11 shows the stability with time of the bimetallic Au_1Cu_1/CeO_2-C and Au_1Cu_1/CeO_2-R catalysts. For each catalyst, the reaction was carried out 3 times. The activity of the Au_1Cu_1/CeO_2-C catalyst is a little bit different in the first run to the subsequent ones, however it then stabilizes and maintains a similar form during the second and the third run. It is worth noting that the activities of Au_1Cu_1/CeO_2-R are similar and stable during the three runs of reaction, suggesting that the reduced bimetallic Au_1Cu_1/CeO_2 catalyst under PROX atmosphere is more stable than that of the calcined one. The time-on-stream performances of the calcined and reduced Au_1Cu_1/CeO_2 bimetallic catalysts collected at 100 °C continuously for a period of 48 h are also shown in Fig. 11 (Inserts). The CO conversion of Au_1Cu_1/CeO_2-C drops significantly after 5 h on-stream. In contrast, a very stable CO conversion was maintained by Au_1Cu_1/CeO_2-R. These results suggest that Au_1Cu_1/CeO_2-R is a more effective and stable catalyst. The deactivation observed on Au_1Cu_1/CeO_2-C could be caused by a variety of factors, including site blockage, surface area decrease due to the presence of carbonates, poisoning of the catalyst surface by the reactants or products. Since the stability obtained is tested at 100 °C, it is unlikely that the
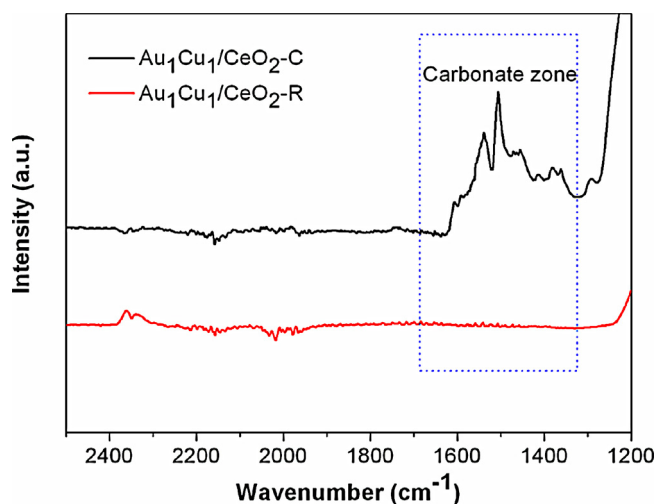
Fig. 12. Investigation of carbonate-like species on used Au_1Cu_1/CeO_2-C and Au_1Cu_1/CeO_2-R catalysts by FT-IR.

sintering of active metals caused its deactivation; this point has been further investigated using FT-IR spectroscopy. The decrease in activity of Au-Cu/CeO$_2$-C catalyst is mainly due to the formation of the carbonate species with bands centred between c.a. 1600–1300 cm^{-1}, species which are not formed on Au-Cu/CeO$_2$-R as shown in Fig. 12.

The best catalyst Au_1Cu_1/CeO_2-R was chosen to study the effect of presence of carbon dioxide and water and their catalytic behaviors are shown in Fig. 13. To mimic more realistic conditions, 10% CO$_2$ and 10% H$_2$O were added to the reactant stream and the H$_2$ concentration was adjusted to 35%. It should be noted that a decrease in hydrogen concentration to 35% instead of 50% can affect the CO conversion [62]. The presence of CO$_2$ decreases the CO conversion as observed by other authors [63]; however, in our case, with the co-existence of CO$_2$ and H$_2$O in the reaction steam, there is no obvious influence on the CO conversion. The addition of water vapor into the feed has a significant positive effect on the reduced Au_1Cu_1 catalyst possibly due to following reasons [64], i.e. (i) enhancement of the WGS reaction and, as a result, more CO is converted into CO$_2$, (ii) hydroxyl groups formed by dissociative adsorption of H$_2$O on gold are also reactive sites, (iii) promotion of the decomposition of carbonates.
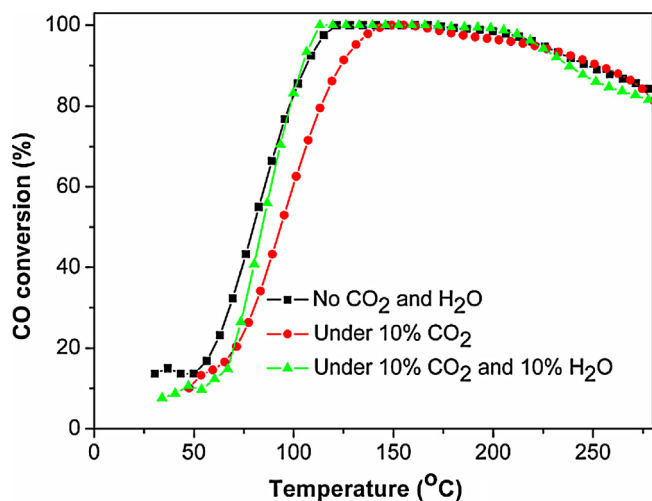

Fig. 13. Resistance toward carbon dioxide and water on Au_1Cu_1/CeO_2-R catalyst (gas composition: 1% CO, 1% O$_2$, 35% H$_2$, 10% CO$_2$ and 10% H$_2$O in He).

4. Conclusions

In this work, the results from X-ray diffraction, high resolution transmission electron microscopy and X-ray photoelectron spectroscopy characterisations have provided important information on the changes of ceria supported bimetallic Au–Cu structures as well as their surface compositions as functions of Cu/Au atomic ratios and thermal treatment atmosphere. The structures of Au–Cu bimetallics are highly dependent upon the Cu/Au ratios and thermal treatments. For calcined bimetallic catalysts, the presence of a copper oxide phase can be observed when the Cu/Au ratio increases from 1/3 to 3/1. For the reduced bimetallic catalysts there is the formation of an Au–Cu alloy and of metallic copper due to immediate decomposition of the copper precursor which can be partially alloyed with gold. From analysis by XPS it was shown that for the calcined catalyst, there is the formation of a Au–CuO phase enriched in CuO or phase-segregated CuO domains enriched on the surface of the support. This phenomenon is strongly dependent upon the Cu/Au atomic ratio. If the bimetallic catalysts are reduced, the amount of enriched-copper on the surface decreases significantly.

The study of the influence of the Cu/Au atomic ratio and thermal treatments on catalytic performance in the CO-PROX reaction indicates that a lower Cu/Au atomic ratio for calcined bimetallic catalysts can promote the catalytic behavior at low reaction temperature (below 100 °C). However, the catalytic behavior of the reduced bimetallic catalysts can be enhanced irrespective of the Cu/Au atomic ratio over the whole range of the reaction temperature and maintained in a wide temperature window with good catalytic performances. A possible explanation for this promoted catalytic behavior by reduced catalysts is related to changes of the bimetallic structure and the decrease in copper of the surface composition. The reduced Au–Cu bimetallics are stable with time on-stream contrary to the calcined one where the formation of carbonate-like species, responsible of a deactivation, is observed. Furthermore the reduced catalyst remained active even in the presence of CO$_2$ and H$_2$O in the gas stream.

References

[1] G. Panzera, V. Modafferi, S. Candamano, A. Donato, F. Frusteri, P.L. Antonucci, Journal of Power Sources 135 (2004) 177.
[2] W. Deng, J. Jesus, H. Saltsburg, M. Flytzani-Stephanopoulos, Applied Catalysis A 291 (2005) 126.
[3] G. Avgouropoulos, M. Manzoli, F. Boccuzzi, T. Tabakova, J. Papavasiliou, T. Ioannides, V. Idakiev, Journal of Catalysis 256 (2008) 237.
[4] M. Manzoli, G. Avgouropoulos, T. Tabakova, J. Papavasiliou, T. Ioannides, F. Boccuzzi, Catalysis Today 138 (2008) 239.
[5] L. Ilieva, G. Pantaleo, I. Ivanov, A. Maximova, R. Zanella, Z. Kaszkur, A.M. Venezia, D. Andreeva, Catalysis Today 158 (2010) 44.
[6] O.H. Laguna, F.R. Sarria, M.A. Centeno, J.A. Odriozola, Journal of Catalysis 276 (2010) 360.
[7] G.Q. Yi, H.W. Yang, B.D. Li, H.Q. Lin, K. Tanaka, Y.Z. Yuan, Catalysis Today 157 (2010) 83.
[8] T. Tabakova, G. Avgouropoulos, J. Papavasiliou, M. Manzoli, F. Boccuzzi, K. Tenchev, F. Vindigni, T. Ioannides, Applied Catalysis B 101 (2011) 256.
[9] J.L. Ayastuy, M.P. Gonzalez-Marcos, A. Gil-Rodriguez, J.R. Gonzalez-Velasco, M.A. Gutierrez-Ortiz, Catalysis Today 116 (2006) 391.
[10] O. Pozdnyakova, D. Teschner, A. Wootsch, J. Krohnert, B. Steinhauer, H. Sauer, L. Toth, F.C. Jentoft, A. Knop-Gericke, Z. Paal, R. Schlogl, Journal of Catalysis 237 (2006) 1.
[11] O. Pozdnyakova-Tellinger, D. Teschner, J. Kroehnert, F.C. Jentoft, A. Knop-Gericke, R. Schlogl, A. Wootsch, Journal of Physical Chemistry C 111 (2007) 5426.

[12] N. Bion, F. Epron, M. Moreno, F. Marino, D. Duprez, Topics in Catalysis 51 (2008) 76.
[13] S.J. Huang, K. Hara, A. Fukuoka, Energy & Environmental Science 2 (2009) 1060.
[14] C.S. Polster, R. Zhang, M.T. Cyb, J.T. Miller, C.D. Baertsch, Journal of Catalysis 273 (2010) 50.
[15] F. Marino, C. Descorme, D. Duprez, Applied Catalysis B 54 (2004) 59.
[16] O. Pozdnyakova, D. Teschner, A. Wootsch, J. Krohnert, B. Steinhauer, H. Sauer, L. Toth, F.C. Jentoft, A. Knop-Gericke, Z. Paal, R. Schlogl, Journal of Catalysis 237 (2006) 17.
[17] A.I. Boronin, E.M. Slavinskaya, I.G. Danilova, R.V. Gulyaev, Y.I. Amosov, P.A. Kumetsov, I.A. Polukhina, S.V. Koscheev, V.I. Zaikovskii, A.S. Noskov, Catalysis Today 144 (2009) 201.
[18] Y.Q. Huang, A.Q. Wang, L. Li, X.D. Wang, D.S. Su, T. Zhang, Journal of Catalysis 255 (2008) 144.
[19] W.P. Dow, Y.P. Wang, T.J. Huang, Journal of Catalysis 160 (1996) 155.
[20] A. Martinez-Arias, A.B. Hungria, M. Fernandez-Garcia, J.C. Conesa, G. Munuera, Journal of Power Sources 151 (2005) 32.
[21] A. Martinez-Arias, A.B. Hungria, G. Munuera, D. Gamarra, Applied Catalysis B 65 (2006) 207.
[22] D. Gamarra, C. Belver, M. Fernandez-Garcia, A. Martinez-Arias, Journal of the American Chemical Society 129 (2007) 12064.
[23] D. Gamarra, G. Munuera, A.B. Hungria, M. Fernandez-Garcia, J.C. Conesa, P.A. Midgley, X.Q. Wang, J.C. Hanson, J.A. Rodriguez, A. Martinez-Arias, Journal of Physical Chemistry C 111 (2007) 11026.
[24] T. Caputo, L. Lisi, R. Pirone, G. Russo, Applied Catalysis A 348 (2008) 42.
[25] A. Gomez-Cortes, Y. Marquez, J. Arenas-Alatorre, G. Diaz, Catalysis Today 133 (2008) 743.
[26] H.C. Lee, D.H. Kim, Catalysis Today 132 (2008) 109.
[27] F. Marino, B. Schonbrod, M. Moreno, M. Jobbagy, G. Baronetti, M. Laborde, Catalysis Today 133 (2008) 735.
[28] A. Martinez-Arias, D. Gamarra, M. Fernandez-Garcia, A. Hornes, P. Bera, Z. Koppany, Z. Schay, Catalysis Today 143 (2009) 211.
[29] D. Gamarra, M. Fernandez-Garcia, C. Belver, A. Martinez-Arias, Journal of Physical Chemistry C 114 (2010) 18576.
[30] E. Moretti, L. Storaro, A. Talon, M. Lenarda, P. Riello, R. Frattini, M.D.M. de Yuso, A. Jimenez-Lopez, E. Rodriguez-Castellon, F. Ternero, A. Caballero, J.P. Holgado, Applied Catalysis B 102 (2011) 627.
[31] T.S. Mozer, D.A. Dziuba, C.T.P. Vieira, F.B. Passos, Journal of Power Sources 187 (2009) 209.
[32] J.C. Bauer, D. Mullins, M.J. Li, Z.L. Wu, E.A. Payzant, S.H. Overbury, S. Dai, PCCP 13 (2011) 2571.
[33] J. d.S.L. Fonseca, L. Pirault-Roy, D. Duprez, F. Epron, Catalysis Today 180 (2012) 34.
[34] X.Y. Liu, A.Q. Wang, T. Zhang, D.S. Su, C.Y. Mou, Catalysis Today 160 (2011) 103.
[35] A. Sandoval, A. Aguilar, C. Louis, A. Traverse, R. Zanella, Journal of Catalysis 281 (2011) 40.
[36] J. Knudsen, L.R. Merte, G.W. Peng, R.T. Vang, A. Resta, E. Laegsgaard, J.N. Andersen, M. Mavrikakis, F. Besenbacher, ACS Nano 4 (2010) 4380.
[37] K. Qian, W.X. Huang, Catalysis Today 164 (2011) 320.
[38] A.U. Nilekar, S. Alayoglu, B. Eichhorn, M. Mavrikakis, Journal of the American Chemical Society 132 (2010) 7418.
[39] S. Monyanon, S. Pongstabodee, A. Luengnaruemitchai, Journal of Power Sources 163 (2006) 547.
[40] B.S. Caglayan, I.I. Soykal, A.E. Aksoylu, Applied Catalysis B 106 (2011) 540.
[41] H. Xu, Q. Fu, Y. Yao, X. Bao, Energy and Environmental Science 5 (2012) 6313.
[42] X.Y. Liu, A.Q. Wang, L. Li, T. Zhang, C.Y. Mou, J.F. Lee, Journal of Catalysis 278 (2011) 288.
[43] J. Llorca, M. Dominguez, C. Ledesma, R.J. Chimentao, F. Medina, J. Sueiras, I. Angurell, M. Seco, O. Rossell, Journal of Catalysis 258 (2008) 187.
[44] S. Ivanova, C. Petit, V. Pitchon, Applied Catalysis A 267 (2004) 191.
[45] S. Ivanova, V. Pitchon, C. Petit, H. Herschbach, A. Van Dorsselaer, E. Leize, Applied Catalysis A 298 (2006) 203.
[46] Y. Azizi, C. Petit, V. Pitchon, Journal of Catalysis 269 (2010) 26.
[47] R.J. Chimentao, F. Medina, J.L.G. Fierro, J. Llorca, J.E. Sueiras, Y. Cesteros, P. Salagre, Journal of Molecular Catalysis A: Chemical 274 (2007) 159.
[48] Z.G. Liu, R.X. Zhou, X.M. Zheng, Journal of Molecular Catalysis A: Chemical 267 (2007) 137.
[49] A.A. Fonseca, J.M. Fisher, D. Ozkaya, M.D. Shannon, D. Thompsett, Topics in Catalysis 44 (2007) 223.
[50] Y.B. Tu, J.Y. Luo, M. Meng, G. Wang, J.J. He, International Journal of Hydrogen Energy 34 (2009) 3743.
[51] Z. Zsoldos, F. Garin, L. Hilaire, L. Guczi, Journal of Molecular Catalysis A: Chemical 111 (1996) 113.
[52] A. Palermo, F.J. Williams, R.M. Lambert, Journal of Physical Chemistry B 106 (2002) 10215–10219.
[53] K.S. Nagabhushana, C. Weidenthaler, S. Hocevar, D. Strmcnik, M. Gaberscek, A.L. Antozzi, G.N. Martelli, Journal of New Materials for Electrochemical Systems 9 (2006) 73.
[54] E.B. Fox, S. Velu, M.H. Engelhard, Y.H. Chin, J.T. Miller, J. Kropf, C.S. Song, Journal of Catalysis 260 (2008) 358.
[55] R.J.K. Wiltshire, C.R. King, A. Rose, P.P. Wells, H. Davies, M.P. Hogarth, D. Thompsett, B. Theobald, F.W. Mosselmans, M. Roberts, A.E. Russell, PCCP 11 (2009) 2305.
[56] Y.C. Wei, C.W. Liu, W.J. Chang, K.W. Wang, Journal of Alloys and Compounds 509 (2011) 535.
[57] M.M. Schubert, M.J. Kahlich, G. Feldmeyer, M. Huttner, S. Hackenberg, H.A. Gasteiger, R.J. Behm, PCCP 3 (2001) 1123.
[58] C.L. Bracey, A.F. Carley, J.K. Edwards, P.R. Ellis, G.J. Hutchings, Catalysis Science & Technology 1 (2011) 76.
[59] K. Balakrishnan, J. Schwank, Journal of Catalysis 138 (1992) 491.
[60] H.H.C.M. Pinxt, B.F.M. Kuster, D.C. Koningsberger, G.B. Marin, Catalysis Today 39 (1998) 351.
[61] S.R. de Miguel, M.C. Roman-Martinez, E.L. Jablonski, J.L.G. Fierro, D. Cazorla-Amoros, O.A. Scelza, Journal of Catalysis 184 (1999) 514.
[62] C. Galletti, S. Specchia, G. Saracco, V. Specchia, Industrial and Engineering Chemistry Research 47 (2008) 5304.
[63] C. Galletti, S. Fiorot, G. Saracco, V. Specchia, Chemical Engineering Journal 134 (2007) 45.
[64] X. Liao, W. Chu, X. Dai, V. Pitchon, Applied Catalysis A 449 (2012) 131.